Constructing a 22-Year Internal Wave Dataset for the Northern South China Sea: Spatiotemporal Analysis Using MODIS Imagery and Deep Learning

5 Xudong Zhang[1, 2], Xiaofeng Li[1, 2*]

[1] Key Laboratory of Ocean Observation and Forecasting
[2] Key Laboratory of Ocean Circulation and Waves, Institute of Oceanology, Chinese Academy of Sciences, Qingdao, China

Correspondence to: Xiaofeng Li (lixf@qdio.ac.cn)

Abstract Internal waves (IWs) are an important ocean phenomenon facilitating energy transfer between multiscale ocean
10 processes. Understanding such processes necessitates the collection and analysis of extensive observational data. IWs predominantly occur in marginal seas, with the South China Sea (SCS) being one of the most active regions, characterized by frequent and large-amplitude IW activities. In this study, we present a comprehensive IW dataset for the northern SCS, covering the area from 112.40°E to 121.32°E and from 18.32°N to 23.19°N, spanning the period from 2000 to 2022 with a 250 m spatial resolution. During the 22 years, a total of 15830 MODIS images were downloaded for further processing. Out
15 of these, 3085 high-resolution MODIS true-color images were identified to contain IW information and were included in the dataset with precise IW positions extracted using advanced deep learning techniques. IWs in the northern SCS are categorized into four regions based on extracted IW spatial distributions. This classification enables detailed analyses of IW characteristics, including their spatial and temporal distributions across the entire northern SCS and its specific sub-regions. Interestingly, our temporal analysis reveals characteristic "double-peak" patterns aligned with the lunar day, highlighting the strong connection
20 between IWs and tidal cycles. Furthermore, our spatial analysis identifies two IW Quiescent Zones within the IW clusters influenced by underwater topography, highlighting regional variations in IW characteristics and suggesting underlying mechanisms merit further investigation. There are also three gap regions between distinct IW clusters, which may indicate different IW sources. The constructed dataset holds significant potential for studying IW-environment interactions, developing monitoring and prediction models, validating numerical simulations, and serving as an educational resource to promote
25 awareness and interest in IW research.

1 Introduction

Oceanic internal waves (IWs) are prominent phenomena in marginal seas and continental shelf areas, characterized by their long-distance horizontal propagation and large amplitude within stratified waters (Haury et al., 1979; Magalhaes et al., 2020; Magalhaes et al., 2022; Pan et al., 2007; Zhang et al., 2022; Zhao et al., 2014). Their significance lies in their role in transmitting
30 energy between multiscale ocean processes and their critical impact on the ocean environment, acoustics, and underwater

navigation (Jia et al., 2019; Ramp et al., 2022b). IWs manifest as either a periodic wave series with distinct amplitude and crest length or solitary solitons. While the IW crest length extends several hundreds of kilometers, their wavelength in the propagation direction spans only a few hundred meters to a few kilometers. Their isolated nature and infrequent occurrence make these waves difficult to capture. Understanding IWs requires extensive collection and analysis of observational data. Traditional methods using oceanographic instruments are costly, labor-intensive, and unsuitable for large-scale observations due to the submerged nature of IWs.

A viable solution to this challenge is offered by remote sensing techniques benefitting from repeated orbits, large spatial coverage, and cost-efficiency (Li et al., 2008; Zhang et al., 2019). Over the past 20 years, the amount of satellite data has grown exponentially, enabling the construction of an IW dataset at a larger and longer scale. Active satellite sensors can detect the sea surface manifestations of IWs because the convergent and divergent motions they induce modulate the sea surface roughness (Alpers, 1985; Zheng et al., 2001), a predominant factor affecting the backscattering intensity of active microwave sensors, such as the synthetic aperture radar (SAR) (Furtney et al., 2024; Jia et al., 2018; Zhao et al., 2004). Passive satellite sensors, such as radiometers, can also detect the IW-induced sea surface roughness signatures by receiving sunlight reflected by the ocean surface (De Macedo et al., 2023; Hu et al., 2021; Sun et al., 2021). Because passive satellite sensors can provide images with higher temporal resolution, wider image swath, and free access, we mainly use passive satellite sensors for the investigation. For instance, since 2000, data with nearly daily global monitoring at a spatial resolution of 250 m has been provided by the Moderate-resolution Imaging Spectroradiometer (MODIS) onboard the Aqua and Terra satellites, suitable for more in-depth IW investigation since it achieves the best possible balance between orbital duration and spatial coverage (De Macedo et al., 2023).

The advent of cloud computing platforms, like the Earth Observation (EO) Browser from ESA, the WorldView from NASA, and the Google Earth Engine (GEE) from Google, have streamlined the repetitive and arduous image pre-processing steps (e.g., radiometric, atmospheric, and geometric corrections). Therefore, the primary challenge in constructing IW datasets is accurately detecting and obtaining the limited quasi-linear IW features dispersed across extensive satellite observations. Manually extracting the IW crest can reduce errors but significantly increase processing time. Consequently, researchers have developed automated tools to extract IW features from satellite observations. These tools typically employ conventional or semi-automated extraction methods, utilizing basic image processing techniques such as image segmentation and edge detection (Kurekin et al., 2020). However, edge detection algorithms often produce discontinuous edge pixels, which may not represent a complete IW crest. Meanwhile, image segmentation techniques struggle to establish consistent threshold values and require additional processing steps to detect boundary pixels.

In recent years, Deep convolutional neural networks (DCNNs) have showcased their capacity in image pattern classification and have become a dependable tool for extracting accurate pixel-level targets from oceanic remote sensing imagery (Li et al.,

65 2022; Li et al., 2020; Liu et al., 2019; Wang and Li, 2023). Numerous machine-learning techniques have been put forth for the automatic extraction of the IW crest from geostationary optical and space-borne SAR imagery (Bao et al., 2019; Ma et al., 2023; Tao et al., 2022; Zheng et al., 2021). However, these studies have only been tested and validated on individual sensors and limited geographical areas with few images, making them insufficient to create a comprehensive IW database over a long period. Recently, Zhang et al. (2023) developed a robust DCNN-based IWE-Net (IW extraction network) model for
70 automatically extracting IW signatures from several satellite sensors with different spatial resolutions, even in difficult imaging circumstances. Implementing IWE-Net allows for fast and accurate processing of a large volume of satellite images.

The northern South China Sea (SCS) serves as an exceptional natural laboratory for studying IWs of large amplitude (Alford et al., 2015; Bai et al., 2017; Bai et al., 2014; Cai et al., 2012; Guo and Chen, 2014; Liang et al., 2019; Liu and Hsu, 2004;
75 Ramp et al., 2022a). IW propagation characteristics, such as the reflection, refraction, and shoaling process, have been extensively studied in the literature. In addition to active IW activity, the northern SCS is influenced by circulation patterns, eddies, Kuroshio intrusion, and other dynamic processes, which can affect IW characteristics. (Dong et al., 2016; Liu et al., 2014; Liu and Abernathey, 2023; Liu et al., 2022; Liu et al., 2016; Xu et al., 2020). Given the multiscale dynamics and active IW activity, a long-term IW dataset would enhance the study of these interactions. The purpose of this study is to utilize IWE-
80 Net to extract IWs from the complete set of MODIS images spanning 22 years in the northern SCS. Following essential post-processing steps, we create a comprehensive and accessible IW dataset, providing valuable resources for research on various IW life stages and their interactions with surrounding dynamic processes.

The paper is organized as follows: Section 2 describes the satellite images and the deep-learning model; Section 3 presents the
85 results; Section 4 highlights the new findings from the constructed dataset; and Section 5 provides the conclusion and future outlook.

2 Data and Methods

2.1 MODIS Imagery Collection

The MODIS sensors, positioned at approximately 700 kilometers in sun-synchronous orbits, are onboard NASA's Terra and
90 Aqua satellites, launched in December 1999 and May 2002, respectively. These sensors provide near-daily global coverage, capturing imagery over a 2,300-km-wide swath with spatial resolutions ranging from 250 m to 1 km (bands 1 and 2 at 250 m, bands 3–7 at 500 m, and bands 8–36 at 1 km). MODIS data processing involves several steps, including data download, geometric correction, radiometric calibration, atmospheric correction, and re-projection.
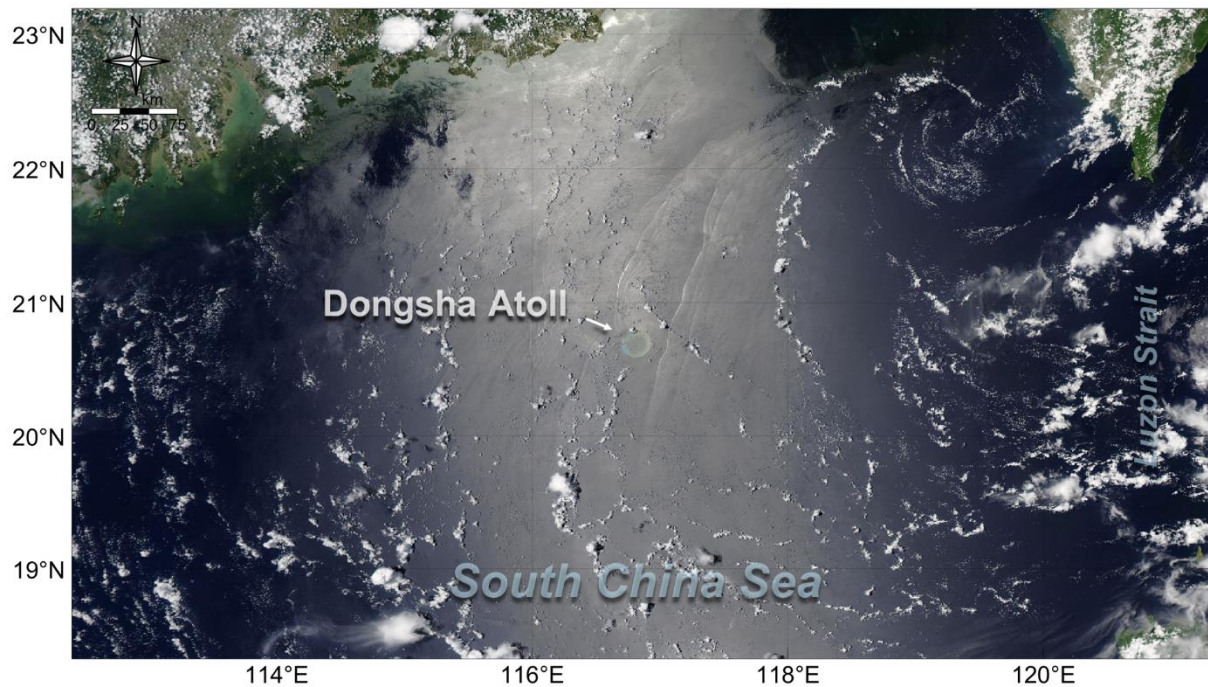
Figure 1. True-color MODIS image captured by Aqua on Jul. 14, 2021, showing IW signatures around Dongsha Atoll in the northern South China Sea.

Through an interactive browsing experience, users can explore global and full-resolution satellite images stored by the Global

100   Image Browse Services (GIBS) system using NASA's Worldview (https://worldview.earthdata.nasa.gov/). The MODIS Corrected Reflectance products (Figure 1) use Level 1B data (calibrated, geolocated radiances) to produce true-color images with three channels: red from band 1, green from band 4, and blue from band 3. This process also involves the removal of significant atmospheric effects, including Rayleigh scattering, to enhance the image quality. Worldview offers Terra MODIS products from Feb. 25, 2000, and Aqua products from Jul. 4, 2002. The target area covers 112.40-121.32°E and 18.32-23.19°N.

105   We collected 15830 MODIS true-color images from 2000 to 2022 as model input, with 8345 from Terra and 7485 from Aqua. All these images have a 250 m spatial resolution and are stored in a GeoTIFF format, which embeds geospatial information into image files.

2.2 Deep Learning Model

The deep-learning model IWE-Net (Zhang et al., 2023) is designed to identify IW locations across a wide range of satellite

110   imagery, including data from both optical and SAR sensors operating in sun-synchronous and geostationary orbits with varying spatial resolutions. This model underwent training and testing using a dataset comprising 1115 satellite images, encompassing 116 full-swath Environmental Satellite (ENVISAT) Advanced SAR (ASAR) images, 839 Terra/Aqua MODIS images, and 160 geostationary Himawari-8 Advanced Himawari Imager (AHI) images. All these satellite images have clear IW signatures

in the SCS, Sulu, and Celebes Sea. Three major improvements are incorporated into IWE-Net to increase its resilience and
115 accuracy: squeeze and excitation blocks, online data augmentation, and the Matthews correlation coefficient loss function,
which takes into consideration the distinct properties of IW under various imaging techniques. The structure of the IWE-Net
is presented in Figure 2.
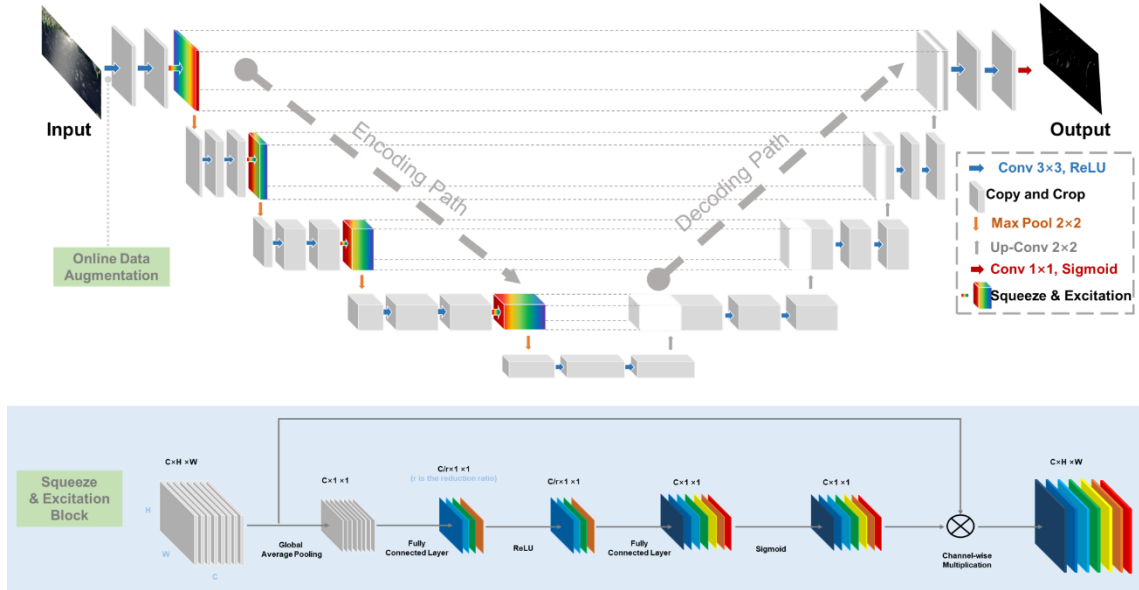
Figure 2. IWE-Net model structure with three tailored modifications adapted from Zhang et al. (2023).

120

We employ the Pixel Accuracy, Precision, Recall, and F1-score as metrics to evaluate the positional differences between the
IW dataset and the ground truths. Pixel Accuracy represents the proportion of the image's pixels that were properly classified.
When there is a significant percentage of negative samples (non-IWs), such as in this task, the Pixel Accuracy often approaches
1 and exhibits a limited responsiveness. Precision, Recall, and F1-score are suitable metrics to evaluate the classifier's output
125 quality when managing uneven classes. Precision reflects the proportion of the false IW pixels in the dataset, while Recall
indicates the proportion of the missed ones. The F1-score is the harmonic mean of these two metrics, balancing Precision and
Recall. The testing set boasts an overall mean precision of 85.75%, a recall of 85.67%, and an F1-score of 85.71%,
demonstrating the model's accuracy in extracting IW signatures.

2.3 Post-processing

130 IWE-Net's performance in the SCS using MODIS images demonstrates an average precision of 87.90%, indicating that around
12% of the model's classifications are false positives. These inaccuracies are primarily due to a small subset of features
resembling IWs, such as aircraft trails, linear and sparse clouds, and surface signals related to shallow water topography and
plumes. These small-scale misclassifications, characterized by their varying shapes and orientations but consistent positions,

can be readily eliminated manually, thus contributing to an overall improvement in the accuracy of this IW dataset. Since the model-produced IW locations are stored in longitude and latitude, users can do more post-processing procedures as needed.

2.5 Data Records

This study generated two sets of data: true-color MODIS Imagery and IW overlay information. All data has been archived and stored in the http://dx.doi.org/10.12157/IOCAS.20240409.001 repository.

- MODIS IW imagery
  - Repository Location: http://dx.doi.org/10.12157/IOCAS.20240409.001
  - Data Format: GeoTIFF. The GeoTIFF format is ideal for storing MODIS imagery of IWs, as it embeds georeferencing information (WGS 84) directly into the file, ensuring accurate pixel-to-geography mapping. Its widespread compatibility with GIS platforms and robust support for large datasets make it a reliable choice for precise and versatile data handling.
  - File Structure:
    - Naming Convention: MODIS_TrueColor_YYYY-MM-DD_SSS.tiff (where YYYY-MM-DD represents the acquisition date of the image and SSS represents the satellite Terra or Aqua)
    - Image Size: 4061 (width) x 2218 (length) pixels
    - Ground pixel Resolution: 250 m x 250 m
    - Data Layers: The following data layers are included:
      - Red channel (Band 1): Data range [0, 255]
      - Green channel (Band 4): Data range [0, 255]
      - Blue channel (Band 3): Data range [0, 255]
    - Georeferencing Information (in the Metadata): Includes projection system, image size, resolution, etc.
- IW Overlay Information
  - Repository Location: http://dx.doi.org/10.12157/IOCAS.20240409.001
  - Data Format: Shapefile. This format excels in archiving IW position data due to its board compatibility with GIS software, enabling seamless interoperability and effective data dissemination. It supports advanced spatial analysis, preserves data integrity, and efficiently manages large datasets for quick and reliable access.
  - File Structure:
    - Naming Convention: IW_YYYY-MM-DD.shp (where YYYY-MM-DD represents the date the IWs occurred)
    - Column Names and Data Types:
      - longitude: Float, precision to 4 decimal places
      - latitude: Float, precision to 4 decimal places

3 IW Signature Extraction and Validation

IWE-Net is an end-to-end model where both input and output are images. It frames IW location extraction as a binary classification, with the output image containing only two values: 1 for IW presence and 0 for non-IW features. Figure 3 illustrates an example of the output and the corresponding input image acquired on Aug. 28, 2002. The extraction results show that most of the IWs are concentrated around the Dongsha Atoll, consistent with the distribution observed in previous studies. In addition, IWE-Net can also effectively identify IWs even in darker regions, as shown in the lower-left part of Figure 3, far from the sun glint area and can barely be visible to the naked eye without image enhancement. It suggests that deep-learning-

based extraction models can potentially exceed the accuracy of visual interpretation, especially when processing large datasets. 3,085 MODIS images containing IW signatures were identified out of the 15,830 input images.

175
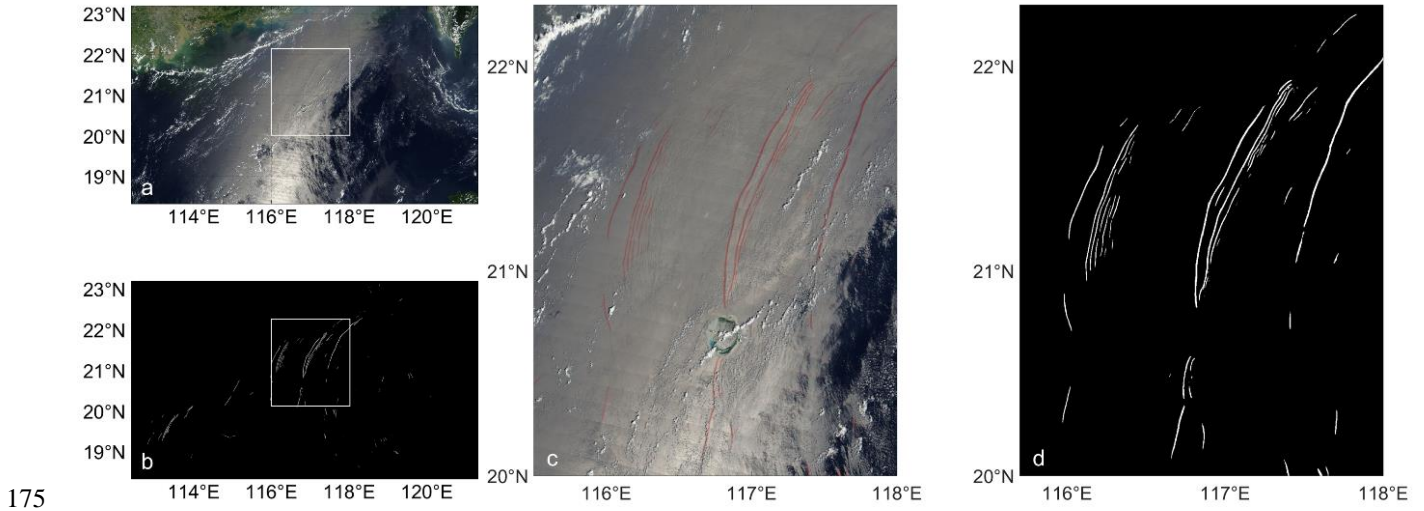
Figure 3. An example of IWE-Net's output (b) alongside the original MODIS image (a) was acquired on Aug. 28, 2002. Panels (c) and (d) show enlarged views of the regions highlighted by the white box in (a) and (b). The red lines in (c) correspond to the white lines in (d).

180   In Figure 3, white points indicate values predicted as 1 by the model, while black points represent predictions of 0, reflecting the precision of IW position detection. However, due to the complex imaging conditions of MODIS in the SCS, no standard IW products are available, and manual extraction remains the most accurate method. We created ground-truth maps based on visual interpretation labels to evaluate the model's performance. A new layer was added to the MODIS image for practical implementation to match the IW reference image size. IW locations were then marked with white lines on a black background.
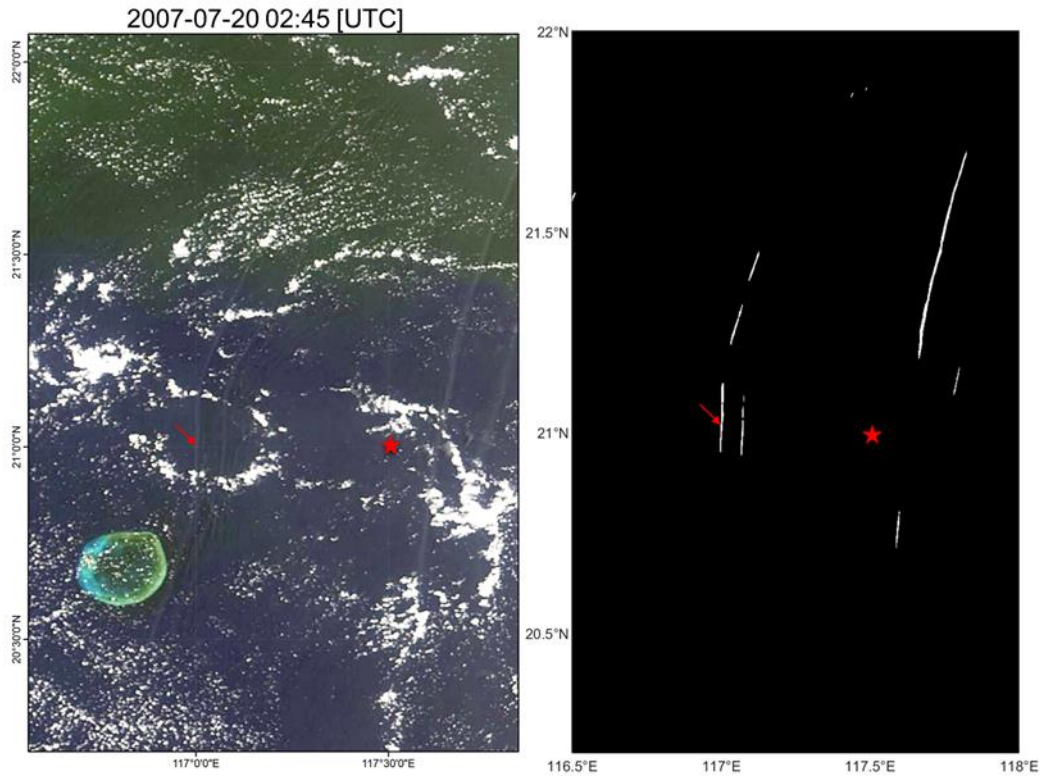
185

Figure 4. The Terra MODS image from Jul. 2007 (left) and corresponding IW locations in the dataset (right). The red star marks the field observation site from Zhao et al. (2012), and the red arrow points to the IW observed in the field study.

Figure 4 illustrates an example of IW detection using a MODIS image captured on Jul. 20, 2007, at 02:45 UTC, alongside
190 field observations detailed by Zhao et al. (2012). The red star marks the locations of the field observations, while the red arrow indicates the IW observed in these field studies. According to Zhao et al. (2012), the IW had several tens of meters amplitude and vertical wave-induced currents exceeding 0.5 m/s (see Figure 3 in their work). This IW was effectively detected through field observations and subsequently captured by the Terra MODIS image approximately 7 hours later. The near-synchronous detection of IWs from satellite imagery and field observations provides strong validation for the accuracy of the applied model
195 and produced dataset.

4 Statistical Analysis

4.1 IW Spatial Distributions in the Northern SCS

We superimpose the IWE-Net-produced IW crest lines using MODIS images from 2000 to 2022 in Figure 5. The spatial resolution of the superimposed map is 250 m, which is the same as the input MODIS image. Most IWs are concentrated around

the Dongsha Atoll, with four distinct clusters in deep and shallow ocean areas. More IWs are generally found in continental shelf regions than in the deep ocean, and their distribution closely aligns with the topographic features.

As shown in Figure 5, we divided the detected IW locations into four regions 1-4, which cover the area from 112.5°E to 114.2°E and from 18.5°N to 20.9°N, from 114.2°E to 118.1°E and from 19.5°N to 22.2°N, from 118.1°E to 120.0°E and from 22.0°N to 23.0°N and from 118.1°E to 120.5°E and from 19.5°N to 22.0°N. The division was based on the geometry of IW crests, indicating different sources for Regions 1 and 3 and various life stages of IWs before and after IWs propagate from the deep ocean to the continental shelf areas in Regions 2 and 4. IWs in Regions 1, 2, and 4 mainly propagate westward, while those in Region 3 propagate southward, suggesting different IW generation sources. More IWs are observed in Region 2 than in Region 4 because the IWs in Region 4 are primarily solitons. As these solitons move into the shallower waters of Region 2, where the depth is less than 1000 meters, they break into multiple IW packets (Li et al., 2013; Ramp et al., 2022b). In addition, the existence of the Dongsha Atoll causes IW reflection or refraction, complicating the IW characteristic (Jia et al., 2018; Li et al., 2013). The IW wave crests in Region 1 do not always align with IWs in Regions 2 and 4, indicating different IW generation sources or mechanisms.
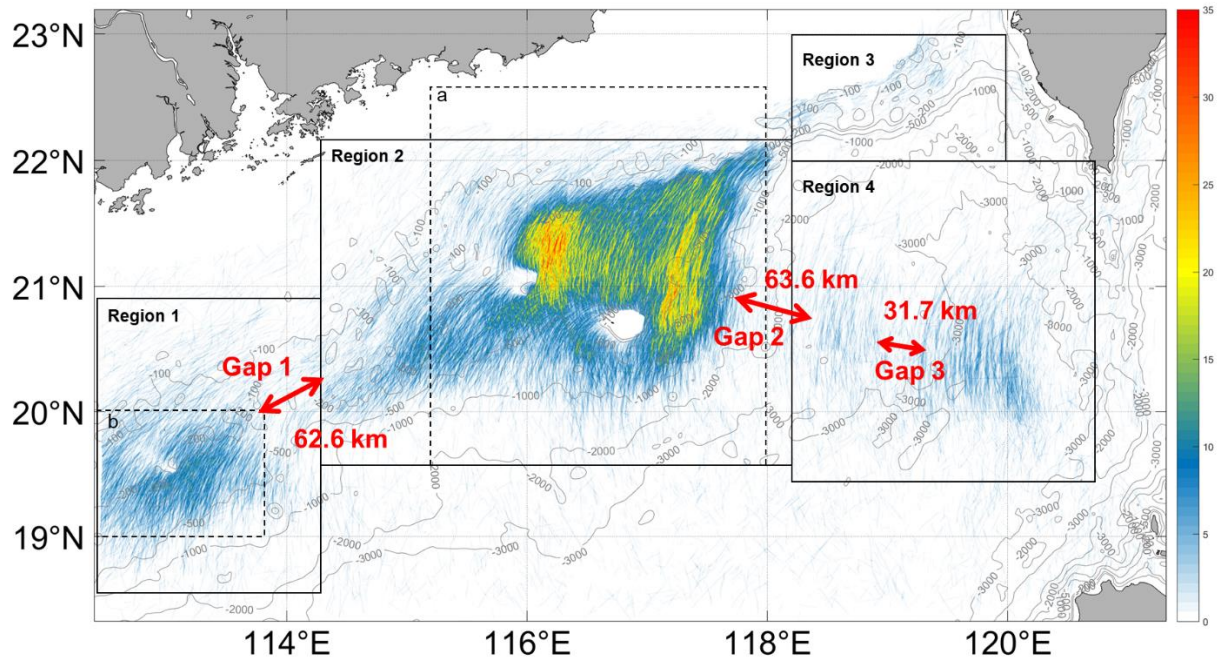
Figure 5. Overlay of IW detection results from MODIS images (2000-2022). Colors represent the frequency of IW observations at each location. The map resolution is 250 m, matching the input MODIS image resolution. Two dashed boxes indicate the locations of the enlarged view (boxes a and b), as shown in Figure 9. Three gaps between different IW clusters and the corresponding spatial distances are labeled with red annotations.
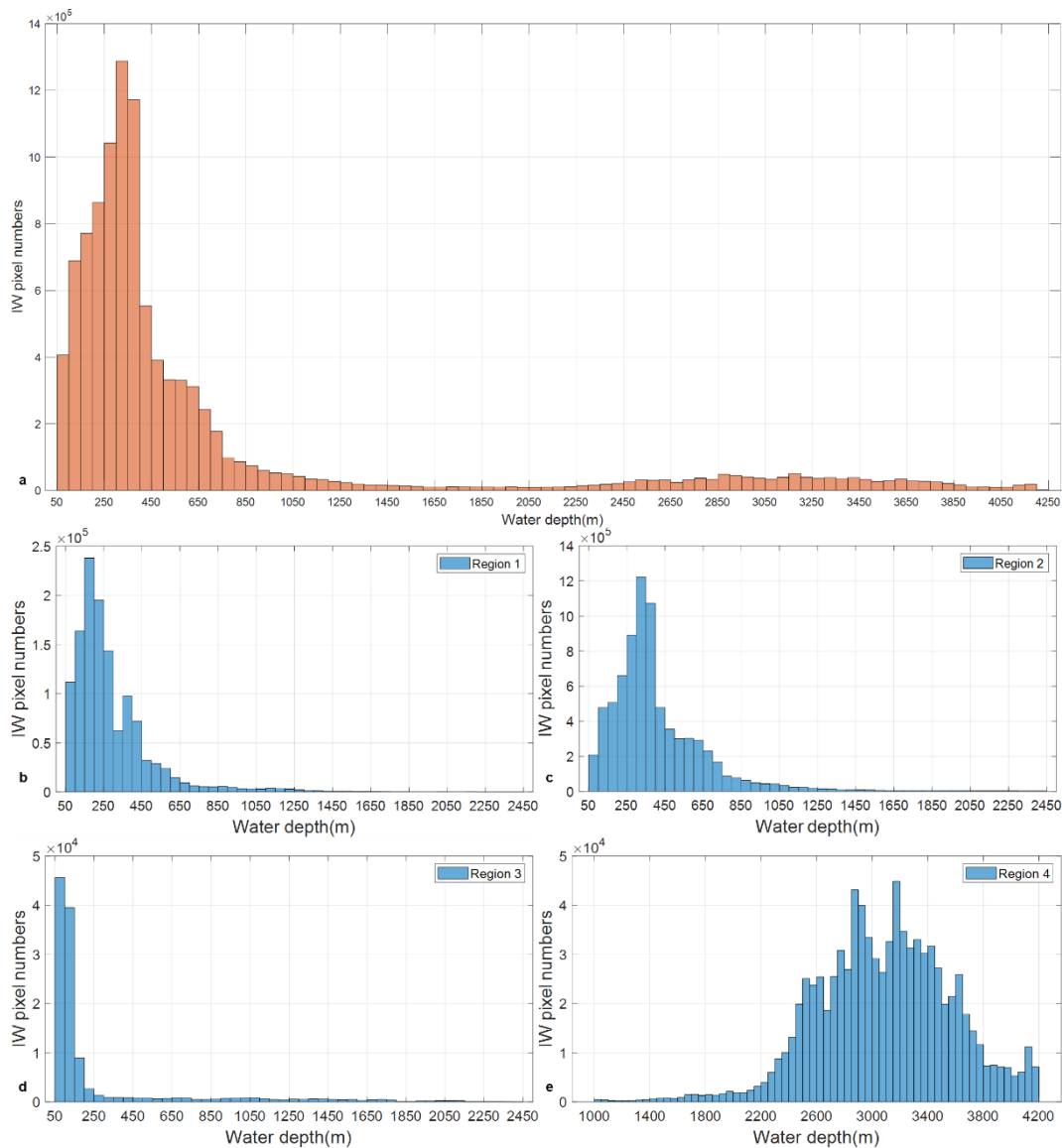
Figure 6. Histograms showing the number of IW pixels versus water depth for (a) the entire northern SCS (orange) and (b-e) the four regions highlighted in Figure 4 (blue).

Underwater topography significantly influences IW evolution. Figure 6 illustrates IW distribution relative to water depth, indicating a prevalence of IWs in open ocean areas with depths under 1000 m. Interestingly, there are more IWs at depths of 3000 m than 2000 m, hinting at an IW evolution mechanism that warrants further study. In Regions 2 and 4 (Figure 4), the distribution of IW clusters corresponds to specific depth characteristics. Region 1 has IWs concentrated at depths less than 600 m despite a total depth range of 100 m to 2000 m. In Region 2, most IWs occur at depths under 1000 m, closely following contours between 100 and 1000 m. In Region 2, most IWs occur at depths under 1000 m, closely following contours between

230 100 m and 1000 m. Region 3 sees IWs primarily at 100 m depths, with their presence decreasing as they move away from the continental shelf and disappearing beyond 2000 m. In Region 4, IWs are mostly found between 2600 to 3600 m, rarely occurring below 2000 m, reflecting a strong correlation between IW distribution and water depth.

4.2 ISW Temporal Distributions-Monthly Variations

Stratification plays a crucial role in IW generation and propagation, with its seasonal variations in the northern SCS causing
235 changes in IW distribution variation. Figure 7 shows that IW occurrences peak from May to August, with significantly fewer detections in other months. This temporal disparity underscores the influence of seasonal changes on the stratification and IW activity. Shallow mixed layer depths and intensified stratification during summer months promote IW activity, enhancing their generation and propagation across the northern SCS. Notably, in Region 3, the distribution is more concentrated in July, suggesting that IWs in this area may require more stringent conditions for generation. In winter, intensified monsoon activity
240 leads to deeper and weaker stratification, reducing the modulation of surface features and making conditions less favorable for IW generation and propagation, resulting in fewer observed IWs. The four classified regions exhibit a similar trend to the entire northern SCS. These findings emphasize the seasonal modulation of stratification and its impact on IW dynamics. They reveal the complex interplay between atmospheric factors like monsoonal circulations and solar radiation in driving seasonal variations in IW activity within the northern SCS.

245
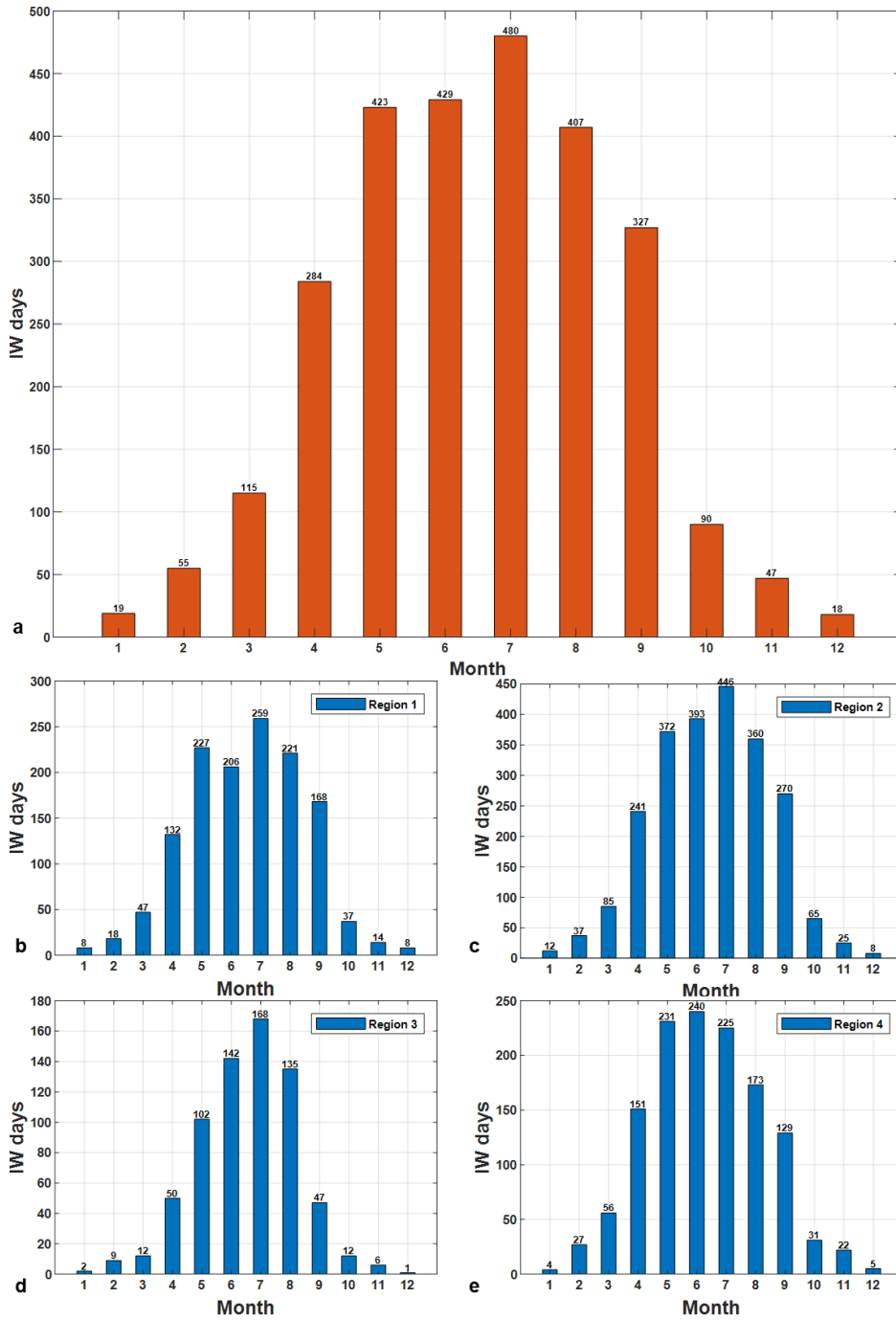
Figure 7. Monthly distributions histograms of IW days for (a) the entire northern SCS (orange) and (b-e) the four regions (blue).

4.3 Lunar Day Influence on IW Variations

The IW generation is closely linked to the astronomical tide, with tidal magnitude directly influencing the IW scale. Astronomical tides follow a fortnightly cycle, peaking on the first and fifteenth lunar days during spring tides. As a result, IW characteristics display fortnightly variations. Figure 8 shows these variations relative to the lunar day, revealing a typical "double-peak" distribution for IWs in the northern SCS. Peak IW occurrences occur approximately four days after the spring tide, as it takes about four days for IWs to travel from the generation site, Luzon Strait, to the observational continental shelf regions before dissipating.

All four regions display a "double-peak" pattern linked to tidal dynamics. Regions 2 and 4 are the main channels for IW in the northern SCS, recording the highest number of IW observation days—446 and 240 days, respectively. In contrast, Region 3 exhibits the fewest IW observation days, with a maximum of just 35 days, suggesting that the generation and propagation of IWs are less favorable in this region. Region 4 exhibits sharper and more defined peaks due to the dominance of IW solitons, whereas Region 2 shows broader peaks typical of IW packet behavior. The shallower water in Region 2 slows IW propagation speed compared to Region 4, resulting in the wider peaks observed.
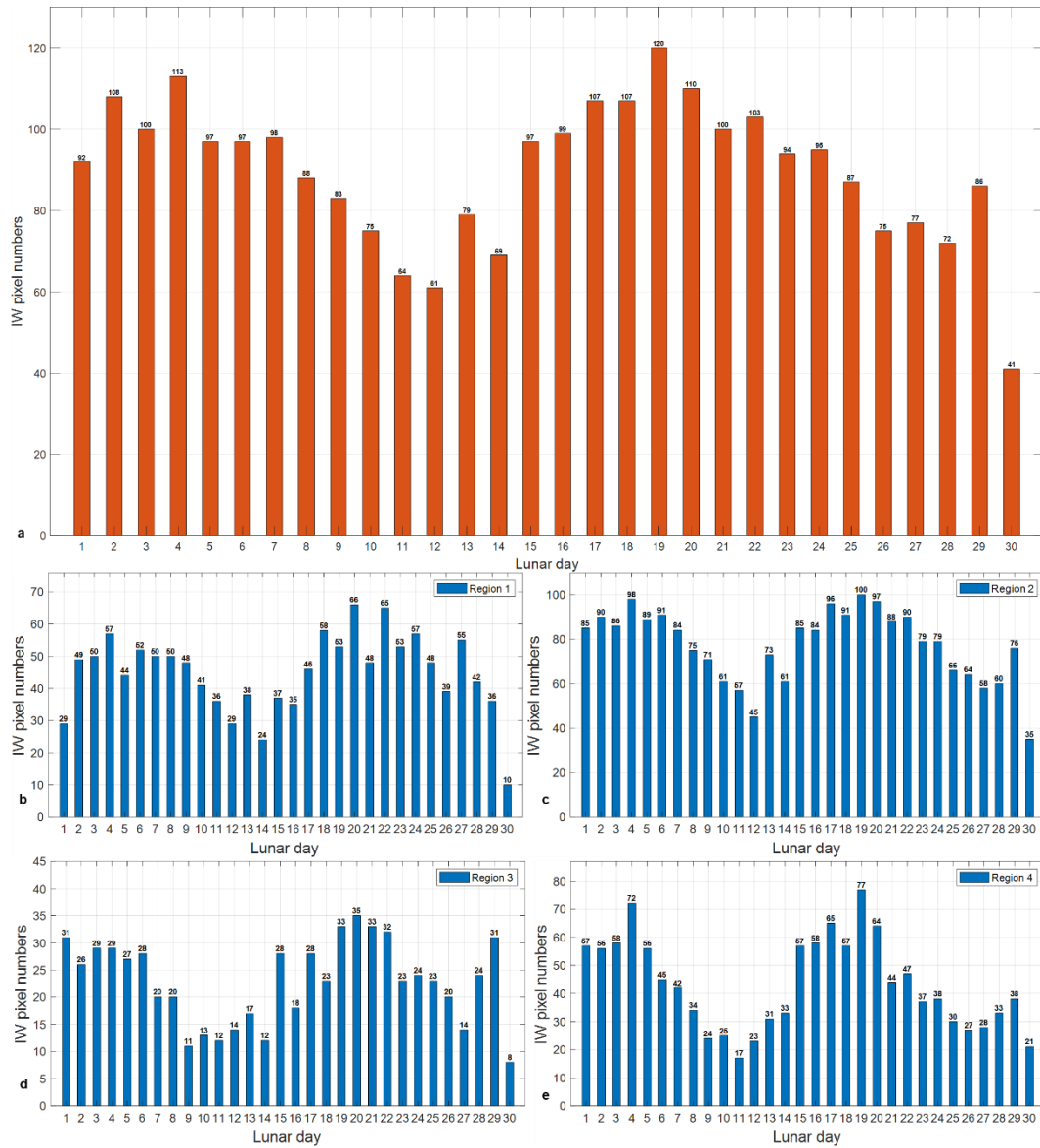
Figure 8. Statistical histograms of IW pixel count vs lunar day for (a) the entire northern SCS (orange) and (b-e) the four regions (blue)

4.4 IW Quiescent Zones

265   Figure 5 shows two distinct blank areas in Regions 1 and 2 within IW clusters. One area in Region 2 covers the well-studied Dongsha Atoll, while the less-known area behind it has received minimal attention in previous research. These blank spaces signify limited or absent IW activity, delineating IW Quiescent Zones. Figure 9 reveals the presence of a chain of small underwater ridges situated in the northwest direction of the Dongsha Atoll. As two black arrows indicate, these ridges

correspond to a series of IW Quiescent Zones. The unique underwater topography contributes to forming IW Quiescent Zones within the northern SCS.

The IW Quiescent Zones adjacent to the Dongsha Atoll extend approximately 110 km towards the continental shelf area, with less than 100 m water depths. Conversely, the IW Quiescent Zones in Region 1 are comparatively smaller, characterized by conspicuous underwater ridges aligned along the direction of IW propagation. These underwater ridges segregate IW crests, with subsequent reconnection occurring at 112.7°E.
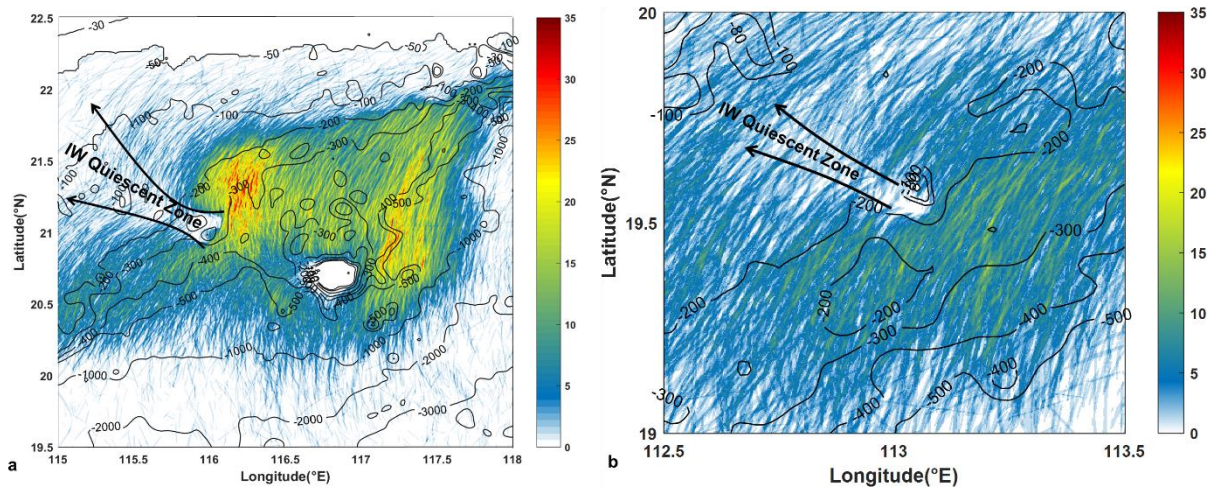
Figure 9. IW Quiescent Zones (black arrows) within IW clusters in Region 2 (a) and Region 1 (b). The locations correspond to two dashed boxes in Figure 5.

IWs exhibit a widespread distribution across the northern SCS, yet noticeable gaps (Gaps 1-3) between distinct IW clusters are evident. Figure 5 shows two IW gap zones, Gap 2 and 3, in Regions 2 and 4, separated by 31.7 km and 63.6 km. The occurrence of Gap 2 and Gap 3 is due to the solitonic nature of IWs, which have fast phase speeds of over 3.0 m/s. The fast propagation of IWs and the observation gaps between two daily MODIS snapshots likely cause Gaps 2 and 3. Additionally, Gap 1, a 62.6 km gap, is clearly observed between Regions 1 and 2, where the differing orientations of IW wave crests suggest distinct IW generation sources. Notably, IW crests show discontinuous features between Regions 2 and 3, coinciding with abrupt underwater topography and small underwater ridges. As a result, IWs originating from different sources undergo separate evolution processes and fail to connect.

5. Conclusion and Outlooks

In this study, we have constructed a comprehensive oceanic IW dataset spanning 2000 to 2022 by applying the deep-learning-based IWE-Net model to MODIS satellite imagery. The model accurately extracts IW locations, providing precise longitude and latitude coordinates of IS crests, which were then compiled into a Shapefile format for easy access and analysis.

The generated IW dataset potentially advances our understanding of IW characteristics in the northern SCS. In the first order, we gain insights into the region's prevalent locations and seasonal variations of IW activity by analyzing the spatial and temporal distributions of IWs based on the collected MODIS images. This dataset also provides valuable information for studying the interactions between IWs and mesoscale ocean phenomena, such as eddies, facilitating further investigations into ocean dynamics (Li et al., 2016; Xie et al., 2016). Cyclonic and anticyclonic mesoscale eddies can cause vertical fluctuations in ocean temperature isopleths and generate accompanying currents, influencing IW characteristics such as amplitude and propagation direction. We can examine IW characteristic changes after passing through different eddy types by analyzing the IW spatial and temporal information provided in this dataset. Additionally, other dynamic ocean phenomena, such as the intrusion of the Kuroshio current, also affect the generation and propagation of IWs in the SCS. Analyzing the statistical characteristics of IWs across different seasons and years can enhance understanding of how dynamic phenomena like the Kuroshio affect the IW behavior, thereby advancing the study of multiscale dynamic interactions in the SCS.

Moreover, the availability of this extensive IW dataset is crucial for advancing artificial intelligence oceanography studies (Li et al., 2022; Wang and Li, 2023). It serves as valuable ground truth data for validating IW generation or forecast models, allowing researchers to assess the performance of AI models by comparing their predictions with the IW locations in the dataset. The dataset can also be used to validate numerical simulations (Gong et al., 2023), enabling researchers to refine and improve these numerical models based on observed IW distributions. It can also serve as a benchmark for collaborative observations of IWs in the SCS with other satellite sensors or field campaigns, thereby facilitating the construction of matched datasets to support IW research with artificial intelligence technologies.

It is important to recognize that the constructed IW dataset has two main sources of error. First, while optical imagery can capture most IW features, weather conditions such as clouds and rain can obstruct MODIS imagery, preventing the detection of IWs even when they are present. Second, the uneven coverage and gaps between polar-orbiting satellites' orbits can lead to missed IW detections in the model's results. Future efforts should consider adding additional satellite sensors, especially SAR imagery, to improve the comprehensiveness of the IW dataset.

Overall, the IW dataset presented in this paper is a valuable resource for oceanography, aiding in studying IW dynamics, validating AI models, and refining numerical simulations. This dataset is expected to stimulate further research and

advancements in understanding the complex dynamics of oceanic IWs. Mooring observations offer vertical structural information on IWs. By integrating this dataset with mooring observation data and applying artificial intelligence technology, researchers can extend from two-dimensional sea surface information to a three-dimensional understanding of IW structure.

6. Data availability

325 The internal wave dataset can be freely downloaded from http://dx.doi.org/10.12157/IOCAS.20240409.001 (Zhang and Li, 2024) or https://datapid.cn/CSTR:33685.11.IOCAS.20240409.001.

Competing interests

The contact author has declared that none of the authors has any competing interests.

Acknowledgements

330 All MODIS images were downloaded from the NASA Worldview application (https://worldview.earthdata.nasa.gov), part of the NASA Earth Observing System Data and Information System (EOSDIS).

Financial support

Xudong Zhang was funded by the National Natural Science Foundation of China (grant nos. U2006211, 42221005, and 41906157).

335 **References**

Alford, M. H., Peacock, T., MacKinnon, J. A., Nash, J. D., Buijsman, M. C., Centurioni, L. R., Chao, S. Y., Chang, M. H., Farmer, D. M., Fringer, O. B., Fu, K. H., Gallacher, P. C., Graber, H. C., Helfrich, K. R., Jachec, S. M., Jackson, C. R., Klymak, J. M., Ko, D. S., Jan, S., Johnston, T. M., Legg, S., Lee, I. H., Lien, R. C., Mercier, M. J., Moum, J. N., Musgrave, R., Park, J. H., Pickering, A. I., Pinkel, R., Rainville, L., Ramp, S. R., Rudnick, D. L., Sarkar, S., Scotti, A., Simmons, H. L., St Laurent,
340 L. C., Venayagamoorthy, S. K., Wang, Y. H., Wang, J., Yang, Y. J., Paluszkiewicz, T., and Tang, T. Y.: The formation and fate of internal waves in the South China Sea, Nature, 521, 65-69, 10.1038/nature14399, 2015.
Alpers, W.: Theory of radar imaging of internal waves, Nature, 314, 245-247, 1985.
Bai, X., Li, X., Lamb, K. G., and Hu, J.: Internal Solitary Wave Reflection Near Dongsha Atoll, the South China Sea, Journal of Geophysical Research: Oceans, 122, 7978-7991, 10.1002/2017jc012880, 2017.
345 Bai, X., Liu, Z., Li, X., and Hu, J.: Generation sites of internal solitary waves in the southern Taiwan Strait revealed by MODIS true-colour image observations, International Journal of Remote Sensing, 35, 4086-4098, 10.1080/01431161.2014.916453, 2014.
Bao, S., Meng, J., Sun, L., and Liu, Y.: Detection of ocean internal waves based on Faster R-CNN in SAR images, Journal of Oceanology and Limnology, 38, 55-63, 10.1007/s00343-019-9028-6, 2019.

350   Cai, S., Xie, J., and He, J.: An Overview of Internal Solitary Waves in the South China Sea, Surveys in Geophysics, 33, 927-943, 10.1007/s10712-012-9176-0, 2012.

de Macedo, C. R., Koch-Larrouy, A., da Silva, J. C. B., Magalhães, J. M., Lentini, C. A. D., Tran, T. K., Rosa, M. C. B., and Vantrepotte, V.: Spatial and temporal variability in mode-1 and mode-2 internal solitary waves from MODIS-Terra sun glint off the Amazon shelf, Ocean Science, 19, 1357-1374, 10.5194/os-19-1357-2023, 2023.

355   Dong, D., Yang, X. F., Li, X. F., and Li, Z. W.: SAR Observation of Eddy-Induced Mode-2 Internal Solitary Waves in the South China Sea, IEEE Transactions on Geoscience and Remote Sensing, 54, 6674-6686, 10.1109/Tgrs.2016.2587752, 2016.

Furtney, S., Romeiser, R., and Graber, H. C.: Automated retrieval of internal wave phase speed and direction from pairs of SAR images with different look directions, Remote Sensing of Environment, 305, 114084, 2024.

Gong, Y., Chen, X., Xu, J., Xie, J., Chen, Z., He, Y., and Cai, S.: An internal solitary wave forecasting model in the northern
360   South China Sea (ISWFM-NSCS), Geoscientific Model Development, 16, 2851-2871, 10.5194/gmd-16-2851-2023, 2023.

Guo, C. and Chen, X.: A review of internal solitary wave dynamics in the northern South China Sea, Progress in Oceanography, 121, 7-23, 10.1016/j.pocean.2013.04.002, 2014.

Haury, L. R., Briscoe, M. G., and Orr, M. H.: Tidally generated internal wave packets in Massachusetts Bay, Nature, 278, 312-317, 10.1038/278312a0, 1979.

365   Hu, B. L., Meng, J. M., Sun, L. N., and Zhang, H.: A Study on Brightness Reversal of Internal Waves in the Celebes Sea Using Himawari-8 Images, Remote Sensing, 13, Artn 3831
10.3390/Rs13193831, 2021.

Jia, T., Liang, J. J., Li, X. M., and Sha, J.: SAR Observation and Numerical Simulation of Internal Solitary Wave Refraction and Reconnection Behind the Dongsha Atoll, Journal of Geophysical Research: Oceans, 123, 74-89, 10.1002/2017jc013389,
370   2018.

Jia, Y., Tian, Z., Shi, X., Liu, J. P., Chen, J., Liu, X., Ye, R., Ren, Z., and Tian, J.: Deep-sea sediment resuspension by internal solitary waves in the northern South China Sea, Scientific Reports, 9, 12137, 10.1038/s41598-019-47886-y, 2019.

Kurekin, A. A., Land, P. E., and Miller, P. I.: Internal Waves at the UK Continental Shelf: Automatic Mapping Using the ENVISAT ASAR Sensor, Remote Sensing, 12, 2476, 10.3390/rs12152476, 2020.

375   Li, Q., Wang, B., Chen, X., Chen, X., and Park, J. H.: Variability of nonlinear internal waves in the South China Sea affected by the Kuroshio and mesoscale eddies, Journal of Geophysical Research: Oceans, 121, 2098-2118, 10.1002/2015jc011134, 2016.

Li, X., Jackson, C. R., and Pichel, W. G.: Internal solitary wave refraction at Dongsha Atoll, South China Sea, Geophysical Research Letters, 40, 3128-3132, 10.1002/grl.50614, 2013.

380   Li, X., Zhao, Z., and Pichel, W. G.: Internal solitary waves in the northwestern South China Sea inferred from satellite images, Geophysical Research Letters, 35, 10.1029/2008gl034272, 2008.

Li, X., Zhou, Y., and Wang, F.: Advanced Information Mining from Ocean Remote Sensing Imagery with Deep Learning, Journal of Remote Sensing, 2022, 1-4, 10.34133/2022/9849645, 2022.

Li, X. F., Liu, B., Zheng, G., Ren, Y. B., Zhang, S. S., Liu, Y. J., Gao, L., Liu, Y. H., Zhang, B., and Wang, F.: Deep-learning-
385   based information mining from ocean remote-sensing imagery, Natl Sci Rev, 7, 1584-1605, 10.1093/nsr/nwaa047, 2020.

Liang, J., Li, X.-M., Sha, J., Jia, T., and Ren, Y.: The Lifecycle of Nonlinear Internal Waves in the Northwestern South China Sea, J Phys Oceanogr, 10.1175/jpo-d-18-0231.1, 2019.

Liu, A. K. and Hsu, M. K.: Internal wave study in the South China Sea using Synthetic Aperture Radar (SAR), International Journal of Remote Sensing, 25, 1261-1264, 10.1080/01431160310001592148, 2004.

390   Liu, B., Li, X., and Zheng, G.: Coastal inundation mapping from bitemporal and dual-polarization SAR imagery based on deep convolutional neural networks, Journal of Geophysical Research: Oceans, 124, 9101-9113, 10.1029/2019jc015577, 2019.

Liu, B., Yang, H., Zhao, Z., and Li, X.: Internal solitary wave propagation observed by tandem satellites, Geophysical Research Letters, 41, 2077-2085, 10.1002/2014GL059281, 2014.

Liu, T. Y. and Abernathey, R.: A global Lagrangian eddy dataset based on satellite altimetry, Earth System Science Data, 15,
395   1765-1778, 10.5194/essd-15-1765-2023, 2023.

Liu, T. Y., He, Y. H., Zhai, X. M., and Liu, X. H.: Diagnostics of Coherent Eddy Transport in the South China Sea Based on Satellite Observations, Remote Sens., 14, 10.3390/rs14071690, 2022.

Liu, T. Y., Xu, J. X., He, Y. H., Lü, H. B., Yao, Y., and Cai, S. Q.: Numerical simulation of the Kuroshio intrusion into the South China Sea by a passive tracer, Acta Oceanologica Sinica, 35, 1-12, 10.1007/s13131-016-0930-x, 2016.

400 Ma, Y. T., Meng, J. M., Sun, L. N., and Ren, P.: Oceanic Internal Wave Signature Extraction in the Sulu Sea by a Pixel Attention U-Net: PAU-Net, IEEE Geosci. Remote Sens. Lett., 20, 10.1109/Lgrs.2022.3230086, 2023.

Magalhaes, J. M., da Silva, J. C. B., and Buijsman, M. C.: Long lived second mode internal solitary waves in the Andaman Sea, Scientific Reports, 10, 10234, 10.1038/s41598-020-66335-9, 2020.

Magalhaes, J. M., da Silva, J. C. B., Nolasco, R., Dubert, J., and Oliveira, P. B.: Short timescale variability in large-amplitude
405 internal waves on the western Portuguese shelf, Cont Shelf Res, 246, 10.1016/j.csr.2022.104812, 2022.

Pan, J., Jay, D. A., and Orton, P. M.: Analyses of internal solitary waves generated at the Columbia River plume front using SAR imagery, J. Geophys. Res.: Oceans, 112, 10.1029/2006jc003688, 2007.

Ramp, S. R., Yang, Y. J., Chiu, C.-S., Reeder, D. B., and Bahr, F. L.: Observations of shoaling internal wave transformation over a gentle slope in the South China Sea, Nonlinear Processes in Geophysics, 29, 279-299, 10.5194/npg-29-279-2022, 2022a.

410 Ramp, S. R., Yang, Y. J., Jan, S., Chang, M. H., Davis, K. A., Sinnett, G., Bahr, F. L., Reeder, D. B., Ko, D. S., and Pawlak, G.: Solitary waves impinging on an Isolated tropical reef: arrival patterns and wave transformation under shoaling, Journal of Geophysical Research: Oceans, 127, 10.1029/2021jc017781, 2022b.

Sun, L., Zhang, J., and Meng, J.: Study on the propagation velocity of internal solitary waves in the Andaman Sea using Terra/Aqua-MODIS remote sensing images, Journal of Oceanology and Limnology, 39, 2195-2208, 10.1007/s00343-020-
415 0280-6, 2021.

Tao, M., Xu, C., Guo, L., Wang, X., and Xu, Y.: An Internal Waves Data Set From Sentinel-1 Synthetic Aperture Radar Imagery and Preliminary Detection, Earth and Space Science, 9, e2022EA002528, 2022.

Wang, H. and Li, X.: DeepBlue: Advanced convolutional neural network applications for ocean remote sensing, IEEE Geoscience and Remote Sensing Magazine, 2023.

420 Xie, J., He, Y., Lü, H., Chen, Z., Xu, J., and Cai, S.: Distortion and broadening of internal solitary wavefront in the northeastern South China Sea deep basin, Geophysical Research Letters, 43, 7617-7624, 10.1002/2016gl070093, 2016.

Xu, J., He, Y., Chen, Z., Zhan, H., Wu, Y., Xie, J., Shang, X., Ning, D., Fang, W., and Cai, S.: Observations of different effects of an anti-cyclonic eddy on internal solitary waves in the South China Sea, Progress in Oceanography, 188, 102422, 10.1016/j.pocean.2020.102422, 2020.

425 Zhang, M., Wang, J., Chen, X., Mei, Y., and Zhang, X.: An experimental study on the characteristic pattern of internal solitary waves in optical remote-sensing images, International Journal of Remote Sensing, 40, 7017-7032, 10.1080/01431161.2019.1597308, 2019.

Zhang, S., Li, X., and Zhang, X.: Internal Wave Signature Extraction from SAR and Optical Satellite Imagery Based on Deep Learning, IEEE Transactions on Geoscience and Remote Sensing, 61, 10.1109/TGRS.2023.3258189, 2023.

430 Zhang, X., Wang, H., Wang, S., Liu, Y., Yu, W., Wang, J., Xu, Q., and Li, X.: Oceanic internal wave amplitude retrieval from satellite images based on a data-driven transfer learning model, Remote Sensing of Environment, 272, 112940, 10.1016/j.rse.2022.112940, 2022.

Zhao, W., Huang, X., and Tian, J.: A new method to estimate phase speed and vertical velocity of internal solitary waves in the South China Sea, Journal of Oceanography, 68, 761-769, 10.1007/s10872-012-0132-x, 2012.

435 Zhao, Z., Liu, B., and Li, X.: Internal solitary waves in the China seas observed using satellite remote-sensing techniques: a review and perspectives, International Journal of Remote Sensing, 35, 3926-3946, 10.1080/01431161.2014.916442, 2014.

Zhao, Z., Klemas, V., Zheng, Q., Li, X., and Yan, X.: Estimating parameters of a two-layer stratified ocean from polarity conversion of internal solitary waves observed in satellite SAR images, Remote Sensing of Environment, 92, 276-287, 10.1016/j.rse.2004.05.014, 2004.

440 Zheng, Q., Yuan, Y., Klemas, V., and Yan, X.-H.: Theoretical expression for an ocean internal soliton synthetic aperture radar image and determination of the soliton characteristic half width, Journal of Geophysical Research: Oceans, 106, 31415-31423, 10.1029/2000jc000726, 2001.

Zheng, Y. G., Zhang, H. S., and Wang, Y. Q.: Stripe detection and recognition of oceanic internal waves from synthetic aperture radar based on support vector machine and feature fusion, Int. J. Remote Sens., 42, 6710-6728,
445 10.1080/01431161.2021.1943040, 2021.